REPORT DOCUMENTATION PAGE

Form Approved
OMB NO. 0704-0188

1. AGENCY USE ONLY (Leave Blank)	2. REPORT DATE 31 March 2004	3. REPORT TYPE AND DATES COVERED Final Report, 1 Jul 00 – 31 Dec 03

4. TITLE AND SUBTITLE
SOOT MORPHOLOGY IN UNSTEADY COUNTERFLOW DIFFUSION FLAMES

5. FUNDING NUMBERS
DAAD19-00-1-0429

6. AUTHOR(S)
William L. Roberts

7. PERFORMING ORGANIZATION NAME(S) AND ADDRESS(ES)
North Carolina State University
Raleigh, NC 27607

8. PERFORMING ORGANIZATION REPORT NUMBER 5-30462

9. SPONSORING / MONITORING AGENCY NAME(S) AND ADDRESS(ES)

U. S. Army Research Office
P.O. Box 12211
Research Triangle Park, NC 27709-2211

10. SPONSORING / MONITORING AGENCY REPORT NUMBER

40185.1-EG

11. SUPPLEMENTARY NOTES
The views, opinions and/or findings contained in this report are those of the author(s) and should not be construed as an official Department of the Army position, policy or decision, unless so designated by other documentation.

12 a. DISTRIBUTION / AVAILABILITY STATEMENT

Approved for public release; distribution unlimited.

12 b. DISTRIBUTION CODE

13. ABSTRACT (Maximum 200 words)

Due to the resulting reduction of efficiency, providing an IR source for tracking and targeting, and its harmful effects on human health, soot emission from diesel engines continues to be of interest to the US Army. The broad focus of this three-year project has been to better understand the soot formation processes occurring in diesel engines though experimentation in simple unsteady counterflow diffusion flames. Specifically, we have developed a planar diagnostic technique to measure the morphology (fractal dimension, primary spherule diameter, number if spherules per aggregate, etc) of soot in a plane using optical techniques, measured soot volume fraction in high pressure jet diffusion flames (up to 30 atmospheres), and measured a range of PAH (three different size classes) in an unsteady counterflow diffusion flame.

14. SUBJECT TERMS
soot morphology, unsteady counterflow diffusion flames, PAH, high-pressure flames, LIF, LII

15. NUMBER OF PAGES
20

16. PRICE CODE

17. SECURITY CLASSIFICATION OR REPORT	18. SECURITY CLASSIFICATION ON THIS PAGE	19. SECURITY CLASSIFICATION OF ABSTRACT	20. LIMITATION OF ABSTRACT
UNCLASSIFIED	UNCLASSIFIED	UNCLASSIFIED	UL

NSN 7540-01-280-5500

Standard Form 298 (Rev.2-89)
Prescribed by ANSI Std. 239-18
298-102

FINAL PROGRESS REPORT

DAAD19-00-1-0429

William Roberts

N. C. State University

31 March 2004

(1) Foreword

Due to the resulting reduction of efficiency, providing an IR source for tracking and targeting, and its harmful effects on human health, soot emission from diesel engines continues to be of interest to the US Army. The broad focus of this three-year project has been to better understand the soot formation processes occurring in diesel engines though experimentation in simple flames. Specifically, we have developed a planar diagnostic technique to measure the morphology of soot in a plane using optical techniques, measured soot formation in high pressure jet diffusion flames, and measured a range of PAH in an unsteady counterflow diffusion flame.

The optical diagnostic technique is an extension of a technique successfully used for point measurements over the last 15 years and yields soot volume fraction and six morphological parameters including primary spherule size and number of spherules per aggregate. We have also investigated an approximation to this technique which requires significantly fewer measurements, and may be applicable to making instantaneous measurements in turbulent flames.

Soot volume fraction was measured in a laminar co-flow jet diffusion flame as a function of pressure, up to 30 atmospheres. Both methane and ethylene were used as fuels, with air as the co-flow. Laser induced incandescence, calibrated with laser extinction, was used to make quantitative soot volume fraction maps, showing the soot yield and spatial distribution are very sensitive to the pressure. These were the first LII measurements in high pressure flames.

Polycyclic aromatic hydrocarbons are the building blocks of soot, and as such dictate the amount of soot formed. By noting that the spectra of laser induced fluorescence from these large molecules is a function of the number of benzene rings, we were able to measure, qualitatively, the concentration of three different sizes of PAHs in an unsteady counterflow diffusion flame. This flame has been extensively studied in our lab, with previous measurements of velocity, temperature, and soot volume fraction under ARO support.

(2) Table of Contents

(3) List of Appendixes, Illustrations and Tables

Figure 1. Soot volume fraction in an ethylene-air co-flow jet diffusion flame. Color scale is linear, with red equal to 13 ppm.

Figure 2. Primary spherule diameter d_p distribution in ethylene-air flame, color scale linear with range between 0 – 46 nm.

Figure 3. Number density of primary particles n_p in ethylene-air flame, linear range with maximum of $1x10^{14}/cm^3$.

Figure 4. Radius of gyration of primary particles Rg in ethylene-air flame, linear range from 0 – 630 nm

Figure 5. Mass fractal dimension in ethylene-air flame, linear range from 0 – 3.

Figure 6. Geometric mean of number of primary spherules per aggregate, Ng, linear range from 0 – 200

Figure 7. Geometric standard deviation of number of primary particles per aggregate, Dn, linear range from 0 – 14.5.

Figure 8. Path averaged soot volume fraction, $f_{sv,avg}$ versus pressure on a log-log scale for methane and ethylene up to 1000 kPa, at 65% and 85% of the flame height.

Figure 9. Emissive power versus pressure on a log-log scale for a methane-air flame at pressures up to 5000 kPa

Figure 10. Soot volume fraction in methane-air flames at various pressures. All images use the same color gradient, but the concentration of soot corresponding to red is unique as follows. (a) P = 0.2 MPa with red equal to 3 ppm, (b) P = 0.4 MPa with red equal to 5 ppm, (c) P = 0.8 MPa with red equal to 20 ppm, (d) P = 1.6 MPa with red equal to 30 ppm, and (e) P = 2.5 MPa and red equal to 40 ppm.

Figure 11. Soot volume fraction in ethylene-air flames at various pressures. All images use the same color gradient, but the concentration of soot corresponding to red is unique as follows. (a) P = 0.1 MPa with red equal to 3 ppm, (b) P = 0.2 MPa with red equal to 10 ppm, (c) P = 0.4 MPa with red equal to 55 ppm, and (d) P = 1.6 MPa with red equal to 300 ppm.

Figure 12 The PAH size class location of methane-air flame at initial strain rate 44 s^{-1} and forcing frequency at 30 Hz.

Figure 13 The PAH zone intensity of methane-air flame at initial strain rate 44 s^{-1} and forcing frequency at 30 Hz.

Figure 14. Non-dimensional responds of PAH class size to non-dimensional forcing frequency showing the responds of large PAH damps more quickly. (Methane)

Figure 15. 15 Non-dimensional responds of PAH class size to non-dimensional forcing frequency showing the responds of large PAH damps more quickly. (Propane)

(4) Statement of the problem studied

Soot Morphology Measurements:

To develop predictive models of the soot formation and destruction processes in turbulent diffusion flames, physical characteristics of the soot, such as primary particle diameter and the number of primary particles per aggregate, must be known. Due to the disturbances in the flowfield and chemistry caused by physical probes, non-intrusive techniques are very desirable. Due to the aggregate nature of soot, neither Rayleigh nor Mie scattering theories are appropriate, and so a relatively new laser light scattering technique was used and modified to derive soot morphology parameters in these unsteady counterflow diffusion flames. This technique relies upon Rayleigh-Debye-Gans / polydisperse fractal aggregate (RDG/PFA) theory to relate optical cross sections, measured at various angles, to the soot's morphology. This technique has been shown to be in excellent agreement with intrusive sampling techniques (TS/TEM) in laminar jet diffusion flames.

In-situ light scattering and extinction measurements have usually been employed in order to obtain critical soot data in flames. Unfortunately, almost all of the early literature inferred soot particle size and number densities using Mie or Raleigh theories using a volume-equivalent diameter. However, since soot is not a sphere, these spherical particle optical theories are unsuitable scattering models for aggregates. The important effect of aggregation on soot optical diagnostics was recognized by the pioneering angular light scattering experiments conducted in the early 70's in laminar and turbulent flames. The main difficulty in the interpretation of these optical measurements was a scattering theory that relates optical cross section to aggregate morphology and size. This obstacle has been overcome by recent developments in fractal concepts. Consequently, several investigators have applied various analysis schemes for obtaining soot aggregate parameters from angularly resolved light scattering and extinction measurements.

In spite of these efforts, however, size and morphology information inferred from in-situ measurements have been limited compared to ex-situ thermophoretic sampling (TS) followed by visual transmission electron microscope (TEM) analysis. In general, these recent studies involved uncertainties in their scattering theories since the effect of particle interactions (multiple scattering) on optical cross sections of aggregates was not known because of limited evaluations. Additionally, there were uncertainties about the soot refractive index, m, at visible wavelengths, and the fractal prefactor, k_f, which relates the number of primary particles in an aggregate, N, to its radius of gyration, R_g, both of which are needed for an accurate inversion. More importantly, these previous studies were usually limited in their general applicability to any aggregating system since they all had various shortcomings in the interpretation of in-situ optical measurements.

Uncertainties in optical theory, refractive index, and fractal prefactor propagate to become uncertainties in the inferred parameters when using optical particulate diagnostics. Consequently, these three ingredients have been studied extensively in the past few years, with the ultimate goal of developing an accurate non-intrusive soot diagnostic method. The Rayleigh-Debye-Gans / polydisperse fractal aggregate (RDG/PFA) theory was found to be a reliable approximation to evaluate the measured optical cross sections of soot aggregates, based on extensive experimental and

computational evaluations. RDG/PFA provides a general approach that yields N_g (geometric mean of number of primary particles per aggregate) and σ_g (for a log-normal distribution), and mass fractal dimension, D_f. This theory also allows determination of the probability density function of N as well as the primary particle diameter, which are the most crucial parameters in particle growth and aggregation studies. Additionally, this aggregate scattering theory, which directly relates aggregate morphology to the various optical cross sections, was assessed for the correct aggregate polydispersity considerations.

This new optical technique was extended from point measurements using a CW laser and photomultiplier tube to planar measurements using a pulsed laser and ICCD camera. These experiments provided instantaneous planar measurements of six morphological parameters and allow the complete characterization of the soot generated in these unsteady laminar diffusion flames. These experiments provide the first measurements of soot morphology in transient diffusion flames, and complement our previous measurements of velocity, temperature, and qualitative OH and PAH concentrations. The output of this research will lead to a better understanding of the soot formation and destruction processes occurring in turbulent diffusion flames. This will lead to more accurate predictive modeling, which will allow the US Army to increase survivability of assets through reduced particulate emissions and reduce life cycle costs through improved fuel efficiency of their Diesel engines.

Unsteady Counterflow Diffusion Flame:

In order to understand the complicated combustion environment inside a Diesel engine, it is first necessary to understand turbulent diffusion flames. These flames are themselves very complex due to the highly non-linear coupling between the fluid dynamics and the chemical kinetics. These three dimensional, unsteady flames have been modeled as an ensemble of strained quasi-steady, one-dimensional laminar flamelets. However, these flamelets are approximations of an inherently unsteady process, and to make a better model, this unsteadiness must be accounted for. We have assembled an unsteady counterflow diffusion flame burner to study the transient effects of unsteady strain rates on the production of soot in propane-air flames.

Using laser based diagnostic techniques, we have mapped the velocity field, quantitative soot volume fraction, qualitative OH and PAH distributions, and the temperature field in these flames. The peak soot volume fraction has been shown to increase by more than a factor of six over the steady flames at some conditions, while decreasing to 10% of the peak at others. The soot volume fraction is insensitive at higher frequencies, while the soot precursor chemistry is still responding to these oscillations.

(5) Summary of the most important results

Planar soot morphology measurements:

To demonstrate that the DRG/PFA technique could be extended from a point technique to a planar technique, a well characterized flame was chosen as the demonstration test bed. A laminar co-flow jet diffusion flame burner, very similar to the now-common Santoro burner, was chosen for the measurements, as there is extensive soot volume fraction and morphology data available in the literature. A 90 mm ethylene diffusion flame was used and the data is shown below. This flame was also chosen because it is very steady, allowing the LII (for f_{sv}) to be measured separately from the scattering. For the LII measurements, the fundamental from an Nd:YAG laser was formed into a laser sheet 20 mm high and approximately 200 microns thick, resulting in a laser fluence of 37.5 MW/cm^2, and signals were collected at 450 nm with a 30 ns gate width with an ICCD camera. These LII measurements were calibrated using laser extinction from a He-Ne laser, and are shown below in Fig X. In the future, this calibration technique will use the un-Q-switched Nd:YAG and an IR camera to get the entire laser extinction profile simultaneously.

To extend the DRG/PFA technique to a planar technique, an appropriate light source and detector had to be chosen. To avoid fluorescence from PAH and incandescence interferences, it was necessary to use a laser fluence much lower than the 37.5 MW/cm^2 used in the LII. Ideally, the fundamental from the Nd:YAG would be used to eleminate any possibility of LIF from PAH, but our ICCD cameras are not sensitive to 1064 nm radiation, and the 2nd harmonic needed to be used. The Nd:YAG was run in long pulse mode (no Q-switch) and the 1 J of IR light was doubled in a BBO crystal. The doubling efficiency was very low due to the low power, resulting in approximately 100 μJ of green, and therefore providing approximately 10 W/cm^2, or six orders of magnitude lower fluence than used in the LII measurements.

Scattering measurements were made at 5° increments between 20° and 160°. Thirty images were averaged and flame illuminosity (primary contributor to the background) was subtracted. The images were also corrected for beam uniformity. The scattering/extinction system was calibrated using Rayleigh scattering from nitrogen. Due to the angle between the laser sheet and the camera, the scattering images were expanded about the centerline by dividing by the sine of the angle. From these 19 sets of images, the following six morphological parameters were determined: primary particle diameter, d_p (nm), shown in Fig. 2, number density of primary particles, n_p (number/cm^3) shown in Fig. 3, radius of gyration of an aggregate, Rg (nm) shown in Fig. 4, mass fractal dimension, D_f, shown in Fig. 5, geometric mean of number of primary particles per aggregate, Ng, shown in Fig. 6, and the geometric standard deviation of number of primary particles per aggregate, Δn, shown in Fig. 7.

To determine the entire seven quantities (the six morphological parameters plus f_{sv}), scattering measurements are required at many angles, the more the better. This is not practical, and not possible in turbulent flames. So, an approximate technique is used where the fractal dimension is assumed to be known. This allows the number of measurements to be reduced to four: two for soot volume fraction (normal incidence and

laser extinction) and scattering at nominally 45° and 135°. One of the objectives of this work was to determine where the assumed technique could be used.

The measured D_f falls within the accepted range of values for mature soot only over a very narrow range. Low in the flame, in the inception zone, the early soot does not behave fractal-like at all, with a measured D_f of less than unity. As these particles are advected upstream and continue to grow and mature, they become more fractal-like. Conversely, the primary spherule diameter reaches a reasonable size fairly early in the flame, with diameters reaching approximately 10 nm at about 25% flame height in the ethylene flames and dropping to near 8 nm at 70% of the flame height before increasing again. The number of spherules per aggregate was observed to increase from approximately 50 at 25% flame height to approximately 250 at 75% flame height. This behavior is expected as the aggregates grow in size through clustering. Thus, techniques and approximations which have been validated for mature soot, are not necessarily appropriate for immature soot.

Soot volume fraction measurements in high pressure flames:

The burner used in this work produces the classic over-ventilated Burke-Schumman laminar diffusion flame. The burner geometry and flow rates were modified several times to achieve a stable laminar flame at elevated pressures. Methane and ethylene were the selected fuels with air as an oxidizer. Ethylene was chosen instead of the more commonly used propane because propane has a low saturation pressure at room temperature and liquefies at pressures even moderately above atmospheric. The inner diameters of the burner's air co-flow and fuel tubes were 37.8 mm and 4.4 mm, respectively. The burner was contained within a water-cooled pressure vessel capable of continuous operation at pressures up to 3.0 MPa. The vessel has a height of 1 m with four protruding flanges, three of which housed windows for observation and non-intrusive diagnostics. The flame was relatively small compared to the volume of the chamber; therefore, air was used to purge the area surrounding the flame and the windows to prevent the accumulation of soot particles along the optical path and water condensation on the windows of the pressure vessel.

The fuel and air flow rates were kept constant as the pressure was increased within the vessel. For the methane-air flame, the fuel flow rate was 0.100 slpm, while the air flow rate was 20.0 slpm. These flow rates produced a flame with a height of approximately 20 mm. The fuel and air flow rates for the ethylene-air flame were 0.060 slpm and 20.5 slpm, respectively.

Observations of the effects of pressure on the physical characteristics of the flame include that the flame was wide and convex at atmospheric pressure, and as the pressure increased, the flame became thinner and more concave. It was also observed that the naturally occurring soot incandescence increased dramatically with pressure. As expected, the ethylene-air flame produced much more soot than the methane-air flame. The transmission of the extinction laser beam decreased dramatically with increasing pressure for the ethylene-air flame. In the ethylene-air flame at pressures of 1.6 MPa and above, soot accumulated around the fuel tube exit. As a consequence, no LII data was taken for the ethylene-air flame above 1.6 MPa. At atmospheric pressure, no LII data was taken for

the methane-air flame as the very low soot loadings did not produce a usable signal to noise ratio.

The 1064 nm output from a Continuum Minilite PIV laser was used to heat the soot particles; this particular wavelength was used to eliminate possible photochemical interferences since the 1064 nm photon is not energetic enough to cause fluorescence of intermediate species, such as PAHs. The output from the laser was formed into a sheet with a height of 37 mm and a thickness of 300 μm prior to entering the region of interrogation. The laser's power was measured, and with the laser sheet dimensions, the laser fluence was found to be 0.30 J/cm^2. A laser fluence of 0.30 J/cm^2 is within the "plateau region" of LII excitation, i.e., above a certain energy threshold, the LII signal emitted from heated soot particles becomes insensitive to the laser fluence.

The LII signal was collected with a Princeton Instruments ICCD camera. A gate width of 30 ns was used in the present work. Careful consideration was given to the filter used with the intensified camera as collection of flame luminosity signal, which is considerable in the higher pressure flames, was to be minimized. It was determined that a 400 nm ± 10 nm filter eliminated the majority of signal due to flame luminosity even with the ethylene flame at 1.6 MPa.

Calibration of the LII signal was accomplished by measuring the extinction ratio of a He-Ne laser. The beam passed through a chopper operating at 300 Hz and a plano-convex focusing lens before reaching two turning mirrors. The first mirror reflected approximately 25% of the beam's intensity through the pressure vessel windows without encountering the flame. This beam accounted for any soot accumulation within the pressure vessel and/or on the windows and any energy fluctuations in the laser beam. The second mirror reflected the remaining beam through the pressure vessel and directly over the center of the fuel tube at a known height above the fuel tube. Before reaching their respective photodiodes, each beam passed through a 632.8 nm laser line filter to eliminate the considerable influence of flame luminosity on the collected signal. An oscilloscope then digitized and temporally averaged the signal collected by the photodiodes.

Since the extinction measurement is an integrated value, the path length must be known accurately. Concurrently with the extinction measurements, images of flame emission were taken with the intensified camera. The exact pixel location of the laser beam's passing was known and the path length was measured at that height. The path length decreased with increasing pressure, indicative of the narrowing effects pressure has on flame shape. The path length of the methane-air flame scaled with pressure as $p^{-0.46}$ and the path length of the ethylene-air flame as $p^{-0.57}$. The extinction measurements were taken at pressures up to 1.0 MPa. Above this pressure, both the methane-air and the ethylene-air flames are no longer considered "optically thin," i.e., the transmission of the laser beam approaches or drops below 80%. The ethylene-air flame rapidly deviates from the condition of being optically thin above pressures of 0.2 MPa.

The calibration procedure requires measuring the extinction ratio of a low-powered laser, knowing an accurate path length, and assuming an axisymmetric flame. It is necessary to use an extinction ratio that corresponds to an optically thin flame. The outcome of the calibration procedure is a calibration factor that relates LII signal intensity to soot volume fraction and ultimately leads to a quantitative image of f_{sv} throughout the

flame. The correction factor found at a pressure yielding an optically thin flame can then be applied to the LII images taken at higher pressures, where the flame is no longer optically thin. The pressure at which this occurs is a function of the fuel.

The extinction measurements collected for the calibration procedure were also used to calculate path averaged f_{sv}, designated as $f_{sv,ave}$, at the same height above the burner where the extinction measurements were taken. The majority of previously reported $f_{sv,ave}$ data taken at elevated pressures has been data of this nature. For comparison, values of $f_{sv,ave}$ were calculated for the methane-air flame at 65% and 85% of the flame height and for the ethylene-air flame at 65% of the flame height. In Fig. 8, $f_{sv,ave}$ is plotted versus pressure on a log-log scale. The slope, m, of the linear fit line can be used to formulate a relationship between soot yield and pressure that states $f_{sv,ave}$ is proportional to p^m. For the methane-air flame at 85% of the flame height, m = 1.1; the methane-air flame at 65% of the flame height, m = 0.77; and the ethylene-air flame at 65% of the flame height, m = 1.75.

Increasing luminosity is indicative of increasing soot presence within a flame. In examining Fig. 9, it becomes evident that two pressure trends are present. The emissive power of the methane-air flame scaled as $p^{1.4}$ for pressures between 0 and 2.5 MPa. As the pressure was increased above 2.5 MPa, the emissive power and, consequently, $f_{sv,ave}$ have a decreased dependence on pressure, $p^{0.2}$.

The LII images were calibrated to an extinction measurement. In this calibration, both signal trapping and laser energy sheet losses were accounted for due to the high soot loading. This methodology uses the unattenuated signal and yields a soot concentration calibration factor that is only influenced by the LII optical system and not by the amount of soot contained within the flame. Briefly, the methodology involved guessing an initial calibration factor, which was used to calculate a corrected soot distribution profile and a corresponding predicted transmission. The predicted transmission was then compared to the experimental transmission found through laser light extinction measurements. A new guess for the calibration factor was chosen and predicted transmissions were calculated and compared to the experimental transmission until a calibration factor was converged upon.

Figure 10 shows the calibrated f_{sv} in the methane flames as a function of pressure from 0.2 to 2.5 MPa. Because f_{sv} increases more than an order of magnitude over this pressure range, the color scale representative of f_{sv} in parts per million (ppm) is not normalized to the same value, i.e., each image is scaled to its particular maximum f_{sv}. The maximum in each image is as follows: 3 ppm at 0.2 MPa, 5 ppm at 0.4 MPa, 20 ppm at 0.8 MPa, 30 ppm at 1.6 MPa, and 40 ppm at 2.5 MPa. Figure 11 shows the calibrated ethylene flames as pressure ranges from 0.1 MPa to 1.6 MPa. The maximum f_{sv} in each of these images is as follows: 3 ppm at 0.1 MPa, 10 ppm at 0.2 MPa, 55 ppm at 0.4 MPa, and 300 ppm at 1.6 MPa. As evidenced, the ethylene flame's soot yield increases by two orders of magnitude as the pressure increases from 0.1 to 1.6 MPa, and is more than an order of magnitude greater than the methane flame at the same pressure. At pressures greater than 1.6 MPa, the ethylene flame is too optically thick to allow any measurements using an optical technique.

As pressure increases, the regions of high soot yield shift. This can be observed when comparing the methane-air flame at 0.8 MPa (Fig. 10-c) and 2.5 MPa (Fig. 10-e). At

0.8 MPa, the peak sooting regions are located on the sides of the flame, and as the pressure increases to 2.5 MPa, the tip of the flame becomes the highest sooting region.

PAH measurements in unsteady counterflow diffusion flame:

Considering the photophysical properties of PAH, many researchers have suggested that the fluorescence at different emission wavelengths could be attributable to specific aromatic structures, i.e., the fluorescence wavelength distribution is dependent on the size of the PAH. Which means that with appropriate spectral filtering, different-sized PAH may be selectively detected. The broad band UV fluorescence centered on 320 nm is from carbonaceous material comprised of two-ring aromatics. The fluorescence spectra peaking in the UV at 300 nm is due to mono-ring aromatics (benzene and derivatives), and spectra peaking in the UV at about 350 nm to two-ring PAH. The fluorescence centered near 400 nm is primarily from small PAH composed of only two to three aromatic rings and fluorescence at 500 or 600 nm arising from larger PAH, typically five rings or more.

The 4th harmonic of the Nd:YAG laser was shaped into a sheet (width 400 μm, height 11 mm) and focused in the center of the burner. 10 mJ of 266 nm radiation, corresponding to a power density of 20 MW/cm^2, was used to excite the PAH with sufficient laser fluency to saturate the transitions under our experimental conditions. An ICCD camera with the set of bandpass filters discussed above was used for LIF collection. For each test run, 100 images were collected at the same experimental condition and averaged in order to smooth laser pulse energy oscillations (minimal due to saturation) and to increase the signal to noise ratio of the measured signal.

In the unsteady counterflow flames, PAH intensity measurements were made at one amplitude and four forcing frequencies, 30, 50, 100 and 200 Hz, with three different initial strain rates: 23, 44 and 74 s^{-1} with both methane and propane fuels. Figure 12 shows the relative position of the different PAH zones in the methane-air flame at initial strain rate 44 s^{-1} and forcing frequency of 30 Hz. Note that the flame is not moving up and down, as both the fuel and air flow rates are oscillating simultaneously, but rather it is the thinning and thickening of the flame as the strain rate first increases and then decreases through the oscillation. This figure shows that the flame is responding to the instantaneous strain rate very well at this low oscillation frequency. Sinusoidal variations in the PAH location continue to respond to the instantaneous strain rate except for the largest PAH class size at 200 Hz. At this high oscillation frequency, the chemical mechanisms responsible for forming the largest PAH do not respond to the fast fluctuations at all. The PAH zone locations in the propane-air flames show a similar pattern, but become unresponsive sooner. The maximum frequency the largest PAH is still responsive is 200 Hz for the initial strain rates of 23 s^{-1} and 44 s^{-1}, but only to 100 Hz for an initial strain rate of 74 s^{-1}.

Perhaps a better measure of the response of the flame to the instantaneous strain rate is the relative concentration of the various class sizes of PAH. It is expected that each class size will have a different characteristic chemical time, and thus for a given oscillation frequency, the resulting Damköhler number will be different. Figure 13 shows the PAH fluorescence intensity of the three different class sizes in the methane-air flame

at an initial strain rate of 44 s^{-1} and forcing frequency of 30 Hz. As seen in this figure, all three classes are responding to the sinusoidal variation in strain rate. With an initial strain rate of 23 s^{-1}, all three PAH sizes respond to up to the maximum forcing frequency of 200 Hz. But when the initial strain rate is increased to 44 s^{-1}, the PAH intensities only responds to up to 100 Hz forcing frequency. At an initial stain rate of 74 s^{-1}, the smallest PAH respond to up to 100 Hz, the medium size PAH respond to up to 50 Hz, while the largest PAH respond to up to only 30 Hz forcing frequency. For the propane-air flame, the PAH responds to up to 100 Hz forcing frequency at an initial strain rate of 23 s^{-1} for all three sizes. When the strain rate is higher than 23 s^{-1}, the PAH only responds to up to 50 Hz forcing frequency. These correspond nicely with measurements of temperature and OH made by the PI on a previous ARO contract. Both measurements demonstrate the existence of a diffusion-limited frequency response of flames subjected to a time-varying flow field. At the 30 Hz and 50 Hz forcing frequencies, the maximum reaction-zone temperature and the OH-field width were found to respond quasi-steadily. At higher forcing frequencies of 100 and 200 Hz, however, transient behavior is evident from the phase relationship between the imposed sinusoidal strain and the resulting OH-field width and peak temperature.

To show the responsiveness of the PAH to the instantaneous strain rate, the data is plotted in a non-dimensional form, and shown in Figure 14 for the methane-air flame. In this figure, the maximum difference in the instantaneous PAH fluorescence intensity throughout the oscillation is non-dimensionalized by the steady state fluorescence intensity. The frequency is expressed in terms of a non-dimenional Stokes parameter. This parameter η_K is used to correlate the variation in maximum flame temperature and also used to correlate the variation in the reaction-zone width. The non-dimenional Stokes parameter is defined as

$$\eta_K = \left(\frac{\pi \cdot f}{K}\right)^{\frac{1}{2}}$$

f is forcing frequency and K is the cycle mean strain rate. A similar correlation is used here to correlate the variation in the different size class PAH fluorescence intensity. Results for the unsteady propane-air flame are shown in Figure 15. Although the scatter in the data is considerable in these figures, the trends are clear: the response of the larger PAH to frequency is the most damped and the response of the smallest PAH is least damped. This means the chemical mechanisms responsible for small PAH formation will continue to respond to the instantaneous strain rate in a quasi-steady manner at higher frequencies than the larger PAH. This is intuitively obvious, as the presence of small PAH is necessary for the formation of large PAH.

(6) Listing of all publications and technical reports supported under this grant or contract. Provide the list with the following breakout, and in standard format showing authors, title, journal, issue, and date.

(a) Papers published in peer-reviewed journals

Still in process of submitting journal articles, see below.

(b) Papers published in non-peer-reviewed journals or in conference proceedings

1. DeCroix, M.E., Welle, E.J, Xiao, J., and Roberts, W.L., "Calibration of Laser Induced Incandescence in Coflow and Counter Flow Diffusion Flames," Western States Section of the Combustion Institute, UCLA, Los Angeles, CA, Oct. 03.
2. McCrain, L. L. and Roberts, W. L., "The Effects of Elevated Pressure on Soot Formation in Non-Premixed Laminar Diffusion Flames," AIAA 2003-4637, 39th Joint Propulsion Conference, Huntsville, AL, July, 03
3. Xiao. J. and Roberts, W. L., "Soot Morphology in Laminar Diffusion Flames Using a New Planar Light Scattering Technique," AIAA 2003-5091, 39th Joint Propulsion Conference, Huntsville, AL, July, 03
4. DeBruhl, C. D., Echekki, T., Roberts, W. L., "NO_x Measurements in an Unsteady Counterflow Diffusion Flame," 3rd Joint Meeting of the US Sections of the Combustion Institute, Chicago Il., Mar 03.
5. Xiao. J. and Roberts, W. L., "PAHs in Unsteady Counterflow Diffusion Flames," 3rd Joint Meeting of the US Sections of the Combustion Institute, Chicago Il., Mar 03.
6. McCrain, L. L. and Roberts, W. L., "Measurements of Soot Volume Fractions in Laminar Diffusion Flames at Elevated Pressures Using Laser Induced Incandescence," 3rd Joint Meeting of the US Sections of the Combustion Institute, Chicago Il., Mar 03.

(c) Papers presented at meetings, but not published in conference proceedings

1. Xiao, J., and Roberts, W. L., "Soot Morphology in A Laminar Counter-flow Diffusion Flame Derived from RDG/PFA Technique," Fall Technical Meeting, Eastern States Section of The Combustion Institute, Hilton Head, SC, Dec. 01

(d) Manuscripts submitted, but not published

1. J. Xiao and W. L. Roberts, "A Planar Technique for Soot Morphology Measurements in Flames," Applied Optics (to be submitted)
2. J. Xiao and W. L. Roberts, "Soot Morphology Changes due to Transient Strain Rates," Combustion and Flame (to be submitted)

3. J. Xiao, E. Austin and W. L. Roberts, "PAH in Unsteady Counterflow Diffusion Flames," Combustion, Science and Technology, (to be submitted)
4. E. J. Welle, W. L. Roberts, "Correlation of Soot Volume Fraction and Temperature in an Unsteady Counterflow Diffusion Flame," Combustion and Fame (to be submitted)
5. E. J. Welle, W. L. Roberts, C. D. Carter, and J. M. Donbar, "Correlation of Scalar Dissipation Rate and Hydrodynamic Strain Rate in Counter Flow Geometries," Experiments in Fluids (to be submitted)
6. M. E. DeCroix, E. J. Welle, J. Xiao, and W. L. Roberts, "Calibration of Laser Induced Incandescence in Coflow and Counter Flow Diffusion Flames," Combustion Science and Technology (under revision)
7. L. L. McCrain and W. L. Roberts, "Soot Volume Fraction Measurements in High Pressure Jet Diffusion Flames," Combustion and Flame (submitted 10 Sept. 03)
8. J. Xiao and W. L. Roberts, "Morphology of Immature Soot in a Laminar Diffusion Flame," Combustion and Flame (under revision)

(e) Technical reports submitted to ARO

None

(7) List of all participating scientific personnel showing any advanced degrees earned by them while employed on the project

Eric Welle, Ph.D. Topic: "The Frequency Response of Counterflow Diffusion Flames." Status: defended Aug. 2002, and is currently member of technical staff at Sandia National Labs.

Dwayne Debruel, MS. Topic: "NOx formation in a counterflow diffusion flame." Status: defended Aug 2003.

Laura McCrain, MS. Topic: "High pressure soot formation." Status: defended Aug 2003.

Jidong Xiao, Ph.D. Topic: "Effect of Flow Unsteadiness on Soot Morphology." Status: defense anticipated in Fall 04

Nicole Erickson, summer undergraduate RA working on soot formation in high pressure flames, will continue as MS student in Fall 04.

Erika Austin, summer undergraduate RA working on NOx formation in unsteady counterflow diffusion flames, will continue as MS student in Fall 04.

(8) Report of Inventions (by title only)

None to Report

(9) Bibliography

None included

(10) Appendixes

Figure 1

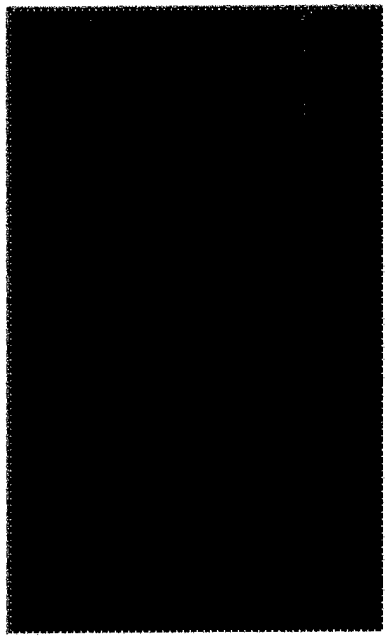

Figure 2

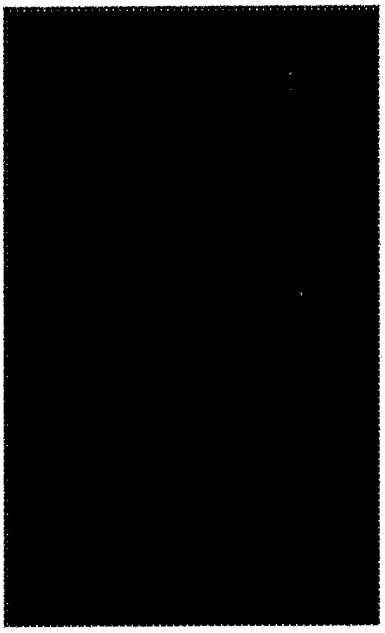

Figure 3

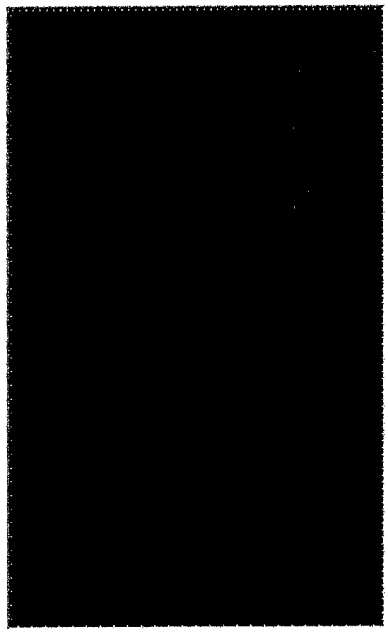

Figure 4

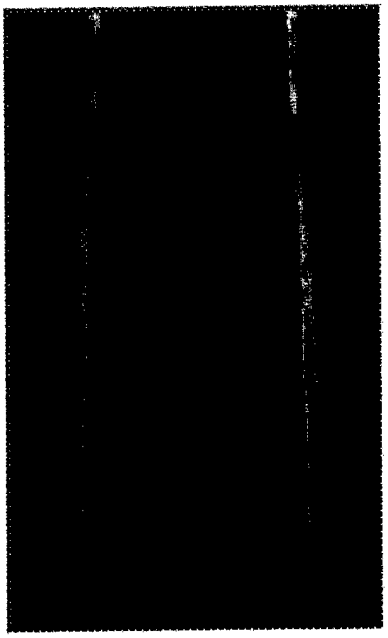

Figure 5

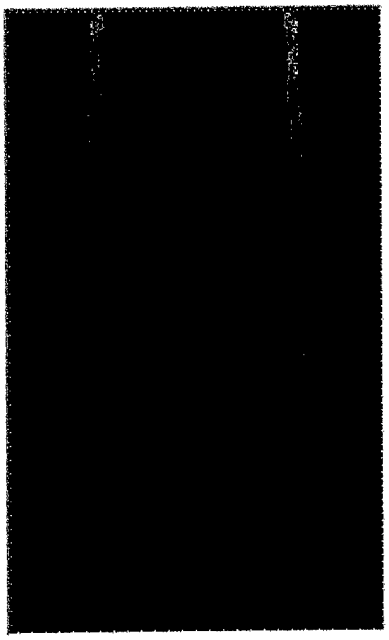

Figure 6

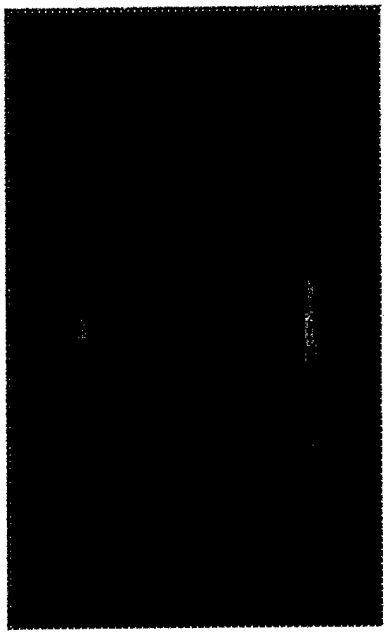

Figure 7

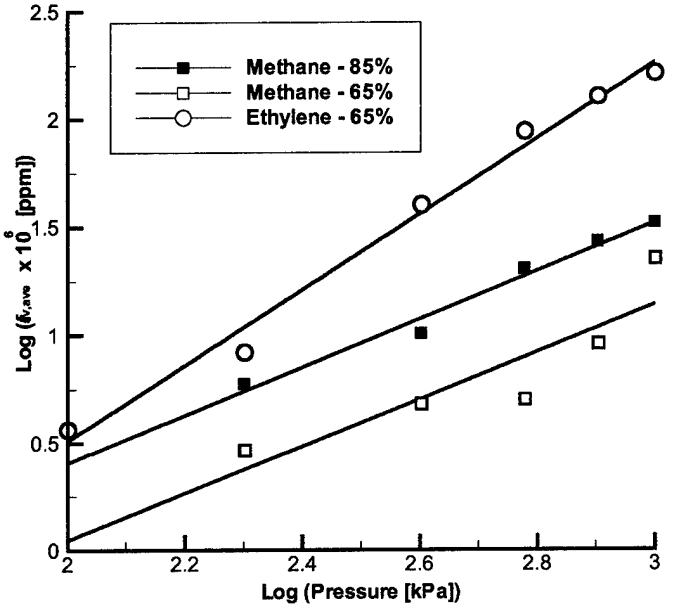

Figure 8

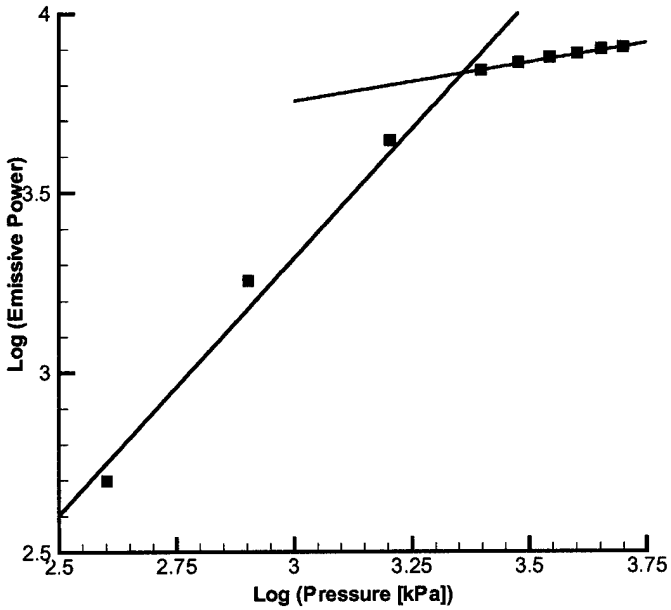

Figure 9

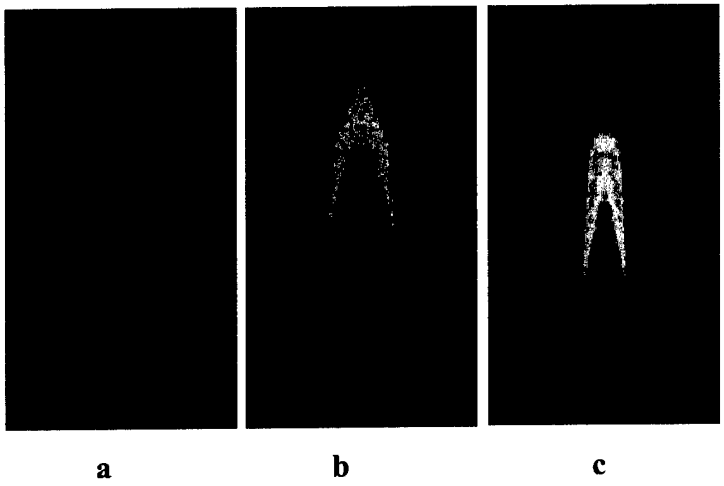

Figure 10

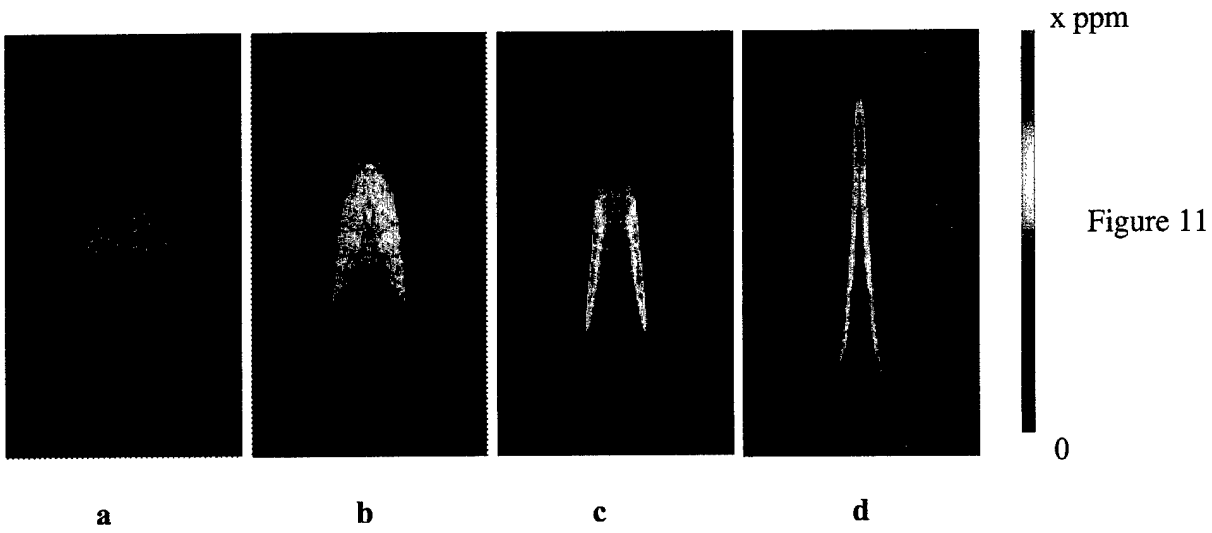

Figure 11

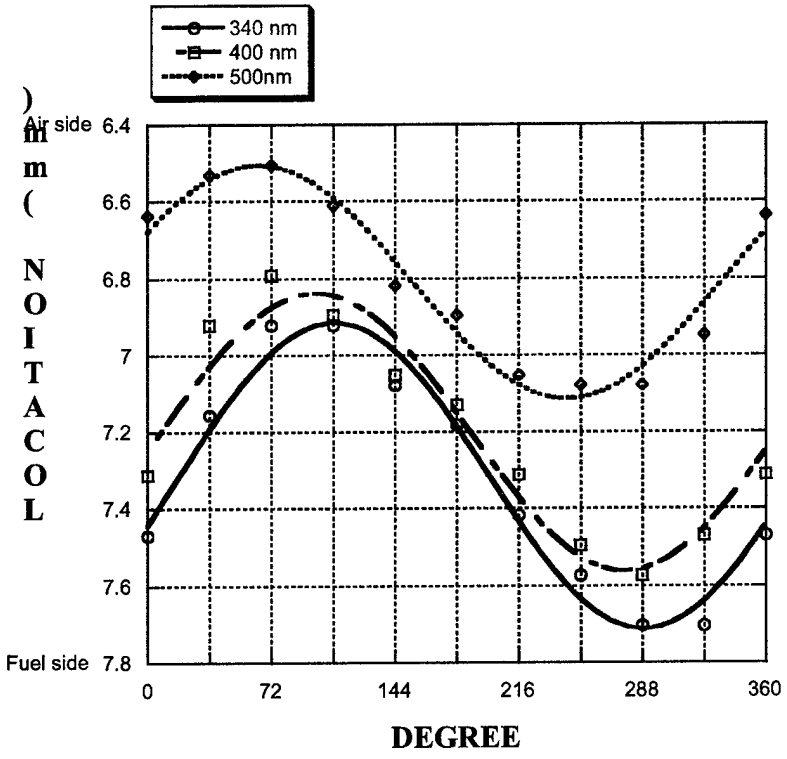

Figure 12

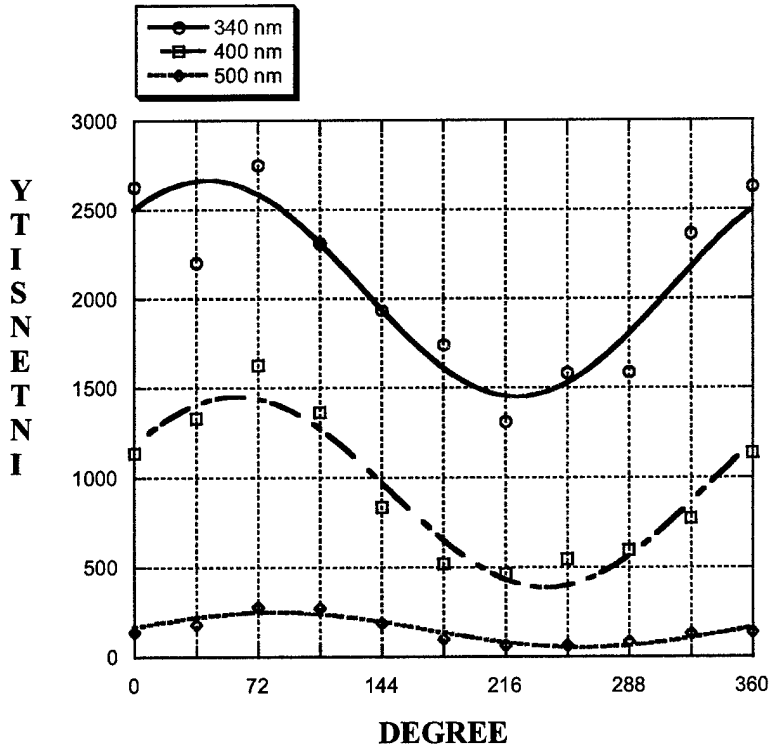

Figure 13

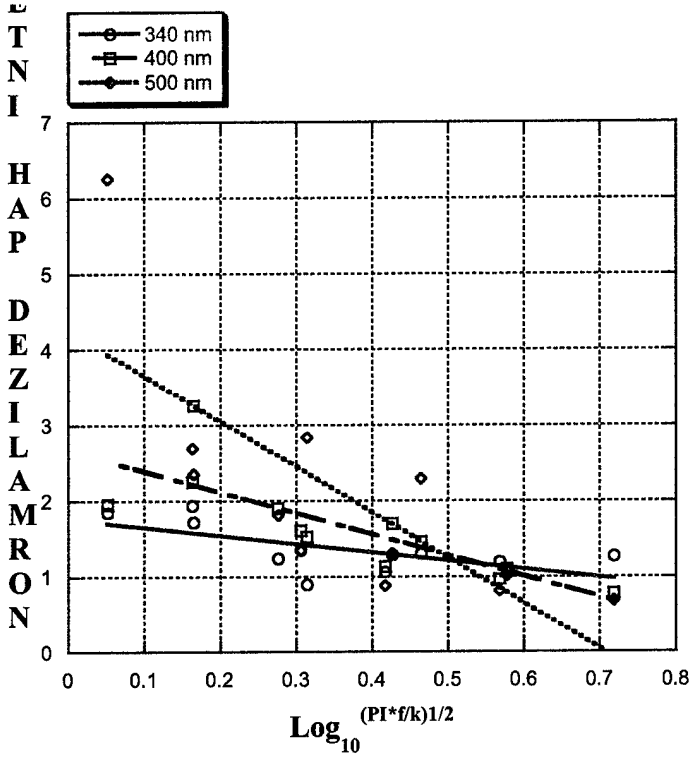

Figure 14

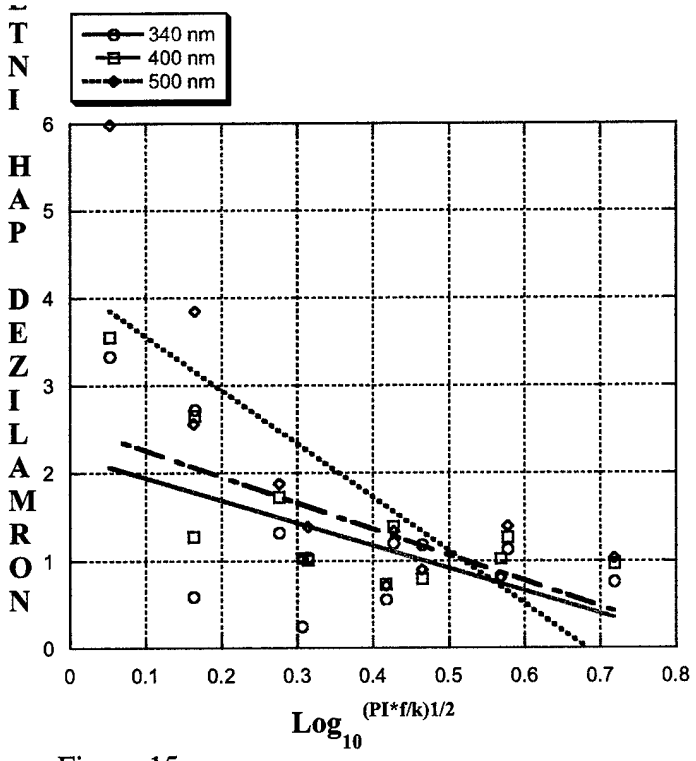

Figure 15